ATMOSPHERIC SCIENCE

# Global concurrent climate extremes exacerbated by anthropogenic climate change

**Sha Zhou[1,2]*, Bofu Yu[3], Yao Zhang[4]**



**Increases in concurrent climate extremes in different parts of the world threaten the ecosystem and our society. However, spatial patterns of these extremes and their past and future changes remain unclear. Here, we develop a statistical framework to test for spatial dependence and show widespread dependence of temperature and precipitation extremes in observations and model simulations, with more frequent than expected concurrence of extremes around the world. Historical anthropogenic forcing has strengthened the concurrence of temperature extremes over 56% of 946 global paired regions, particularly in the tropics, but has not yet significantly affected concurrent precipitation extremes during 1901–2020. The future high-emissions pathway of SSP585 will substantially amplify the concurrence strength, intensity, and spatial extent for both temperature and precipitation extremes, especially over tropical and boreal regions, while the mitigation pathway of SSP126 can ameliorate the increase in concurrent climate extremes for these high-risk regions. Our findings will inform adaptation strategies to alleviate the impact of future climate extremes.**

## INTRODUCTION

A notable number of record-breaking weather and climate extremes, such as heat waves, droughts, and heavy precipitation, have occurred in the past decades (*1*, *2*). These extreme events are often driven by multiple dependent climate drivers, and they can occur simultaneously in different parts of the world, causing severe and, in some cases, irreversible impacts on human and natural systems (*3*, *4*). Although there is a rapidly growing body of literature on temporally co-occurring climate extremes (*3*–*11*), investigation into the spatial co-occurrence of climate extremes has not received much attention (*12*, *13*). In 2021, a record-shattering heat wave blasted large parts of the U.S. Pacific Northwest and Canada at the end of June (*14*), and soon after, deadly heavy precipitation and flooding hit northwestern Europe, China, India, and Afghanistan (*15*, *16*), all of which have caused hundreds of deaths and widespread damage to property and infrastructure and costed billions of dollars in economic losses. These almost simultaneously occurring climate extremes raise serious concerns with a worldwide increase in the extent of concurrent climate extremes and their detrimental impacts on the welfare of human society and ecosystem sustainability.

The socioeconomic impacts of climate extremes are particularly severe when they occur in populous and/or agricultural regions. As the global population grows and cities expand, population at the risk of climate extremes is increasing. Co-occurring heat waves in many urban areas may cause large-scale power outages and increase heat exposure and heat-related mortality (*17*). It is also challenging to deal with concurrent heavy precipitation and floods in large river basins in multiple regions/countries, which lead to widespread infrastructure damage, loss of lives, and other substantial socioeconomic impacts (*15*, *18*, *19*). Spatially concurrent climate extremes may also impose a great risk to the global food supply chain and amplify threats to global food security (*12*, *13*, *20*–*23*). As supply chains are increasingly interconnected, climate-induced production failures in one region may trigger societal impacts in other regions through the trade networks, and simultaneous climate extremes in several agricultural regions may threaten global food security and affect the international financial market (*21*, *23*). Beyond these impacts on our society, co-occurring climate extremes also pose serious threats to terrestrial ecosystems, for example, simultaneous large wildfires associated with hot and dry weather can overwhelm the suppression capacity, leading to greater fire damages and widespread forest mortality and environmental impacts (*24*).

There is mounting evidence to suggest that anthropogenic climate change has led to more frequent and more intense climate extremes over land (*25*–*29*). As climate extremes are emerging over an increasing fraction of land area, co-occurring climate extremes at different locations are expected to be more frequent with $CO_2$-enhanced global warming (*30*). However, the spatial co-occurrence pattern of climate extremes and the extent to which its changes can be attributed to global climate change are unknown. Anthropogenic climate change alters the mean and variability of climate variables as well as the strength of dependence between climate drivers (*4*). We therefore hypothesize that anthropogenic climate change increases the frequency and intensity of spatially concurrent climate extremes through changes in the mean and increases in climate variability and in the spatial dependence of climate extremes. Given the tremendous impacts of spatially co-occurring climate extremes, it is crucial to test the hypothesis for a better understanding of whether and by how much anthropogenic climate change has altered and will continue to affect the spatial co-occurrence of climate extremes around the world.

To gain insight into these questions, we propose a statistical framework to assess the prevalence of spatial co-occurrence of climate extremes at the grid, regional, and global scales, and quantify how the concurrence of extremes changed in the past and is

[1]State Key Laboratory of Earth Surface Processes and Resource Ecology, Faculty of Geographical Science, Beijing Normal University, Beijing, China. [2]Institute of Land Surface System and Sustainable Development, Faculty of Geographical Science, Beijing Normal University, Beijing, China. [3]School of Engineering and Built Environment, Griffith University, Nathan, Queensland, Australia. [4]Sino-French Institute for Earth System Science, College of Urban and Environmental Sciences, Peking University, Beijing, China.
*Correspondence author. Email: shazhou21@bnu.edu.cn

likely to change in the future because of anthropogenic climate forcing. The statistical framework identifies the spatial dependence of climate extremes when the null hypothesis that climate extremes occur independently at two grid cells is rejected at a confidence level of 95% (Materials and Methods). We use monthly climate observations including Climate Research Unit temperature and precipitation products (*31*), Berkeley Earth (BE) temperature product (*32*), and Global Precipitation Climate Center precipitation product (*33*), and an ensemble of 11 General Circulation Models (GCMs) in Coupled Model Intercomparison Project phase 6 (CMIP6) (table S1 and Materials and Methods) (*34*). To better characterize regional co-occurrence, we use the updated Intergovernmental Panel on Climate Change Sixth Assessment Report (IPCC AR6) climate reference regions, which are identified according to consistent regional climate features using observational and modeling (CMIP5 and CMIP6) climate datasets (*35*). We present the global pattern of concurrent climate extremes among 44 land regions (excluding Antarctica; table S2) and identify the hotspot regions where the spatial concurrence of climate extremes is particularly responsive to anthropogenic climate forcing over historical and future periods.

## RESULTS

### Increased global concurrent climate extremes due to anthropogenic climate forcing

To assess the spatial concurrence of climate extremes, we first analyze the proportion of land grid cells (excluding Antarctica) experiencing climate extremes each month over the period 1901–2020. Temperature extremes are defined as months when temperature anomalies relative to the monthly mean values in 1901–2020 are either above their 95th percentiles or below their 5th percentiles, and precipitation extremes are likewise defined. According to this definition, 10% of land grid cells is expected to experience climate extremes for each month of 1901–2020 if they occur independently at different grid cells. Departures from the expected 10%, i.e., either higher or lower than 10%, would therefore indicate the existence of spatial dependence of climate extremes, and the greater the departure, the stronger the spatial dependence.

The observed proportion of land grid cells experiencing simultaneous temperature extremes ranges from 0 to 50% during the period of 1901–2020 (Fig. 1A), which indicates a strong spatial dependence of temperature extremes worldwide. The annual mean proportion of land grid cells with co-occurring temperature extremes remains ~10% in the 20th century and sharply increases to ~20% in the early 21st century (Fig. 1A). This proportion increase is dominated by the proportion of extreme high temperature, while the proportion of extreme low temperature is decreasing (fig. S1, A to D). Consistent with the observations, the historical ensemble from CMIP6 also suggests that land regions become substantially more likely to experience concurrent temperature extremes in the early 21st century (Fig. 1C). However, there is practically no increase in the proportion of land grid cells having co-occurring temperature extremes throughout 1901–2020 in the hist-nat ensemble forced by natural forcing only (Fig. 1C). These results suggest that the observed increases in global concurrent temperature extremes would not have occurred without historical anthropogenic climate forcing.

The spatial dependence of monthly precipitation extremes is also evident, with an observed proportion of land grid cells ranging from 2 to 27% at the monthly scale (Fig. 1B). The annual mean proportion of land grid cells experiencing precipitation extremes increases from ~6 to ~13% in the first 60 years of the 20th century, contributed by increases in both extreme low and extreme high precipitation (fig. S1, E to H). The annual mean proportion is decreased slightly over the past 60 years but remains above 10%. The historical simulations show a relatively stable annual mean proportion of 10% in the 20th century, but the proportion gradually increases to about 11% in the early 21st century (Fig. 1D). In contrast, the probability of precipitation extremes remains centered around 10% throughout the hist-nat simulations (Fig. 1D). The divergent trends between the historical and hist-nat simulations in recent 2 decades indicate that anthropogenic climate forcing may also enhance the risk of global concurrent precipitation extremes.

Anthropogenic climate forcing affects concurrent climate extremes through climate trend and/or variability. With the long-term temperature trends removed, the proportion of observed temperature extremes is reduced greatly, especially in the 21st century, and the difference between the hist-nat and historical ensembles is also reduced noticeably (Fig. 1, A, C, and E). This demonstrates that the observed increases in co-occurring temperature extremes are mainly caused by the anthropogenic warming trend. In contrast, the precipitation trend exerts little influence on concurrent precipitation extremes in both observations and model simulations (Fig. 1, B, D, and F). The increasing co-occurring precipitation extremes are mainly induced by increased precipitation variability (fig. S2), which increases the likelihood of crossing precipitation thresholds. The proportion of land grid cells experiencing climate extremes also vary greatly in hist-nat simulations (Fig. 1, C to F). This indicates the widespread existence of spatially co-occurring climate extremes in nature, while anthropogenic climate forcing enhances the strength and extent of spatial co-occurrence of climate extremes around the world.

Continued greenhouse gas emissions are projected to further increase global concurrent climate extremes. In the high-end emission scenario, i.e., Shared Socioeconomic Pathway 5-8.5 (SSP585), the proportion of land grid cells experiencing temperature extremes defined according to historical thresholds are projected to increase from 21% in 2020 to 95% in 2100; during the same period, the proportion for concurrent precipitation extremes doubles from 11 to 22% (Fig. 1, C and D). The lower forcing in the SSP126 scenario substantially reduces the projected proportion to 43% for temperature extremes and 13% for precipitation extremes in 2100 (Fig. 1, C and D). These model projections indicate that climate extremes will co-occur in more regions, depending on the greenhouse gas emission pathways. It is therefore crucial to further identify the spatial patterns of co-occurring climate extremes in current and future climate and determine the hotspot regions where climate extremes are becoming increasingly co-dependent at different levels of anthropogenic climate forcing.

### Global pattern of spatially concurrent climate extremes

We develop a statistical framework for assessing the spatial concurrence of climate extremes at the grid, regional, and global scales (Materials and Methods). The concurrence probability of climate extremes is identified according to the dependence of climate extremes at different land grid cells (2° × 2°). For a pair of grid cells, if their climate extremes are tested to be positively or negatively dependent, we calculate the associated concurrence probability of

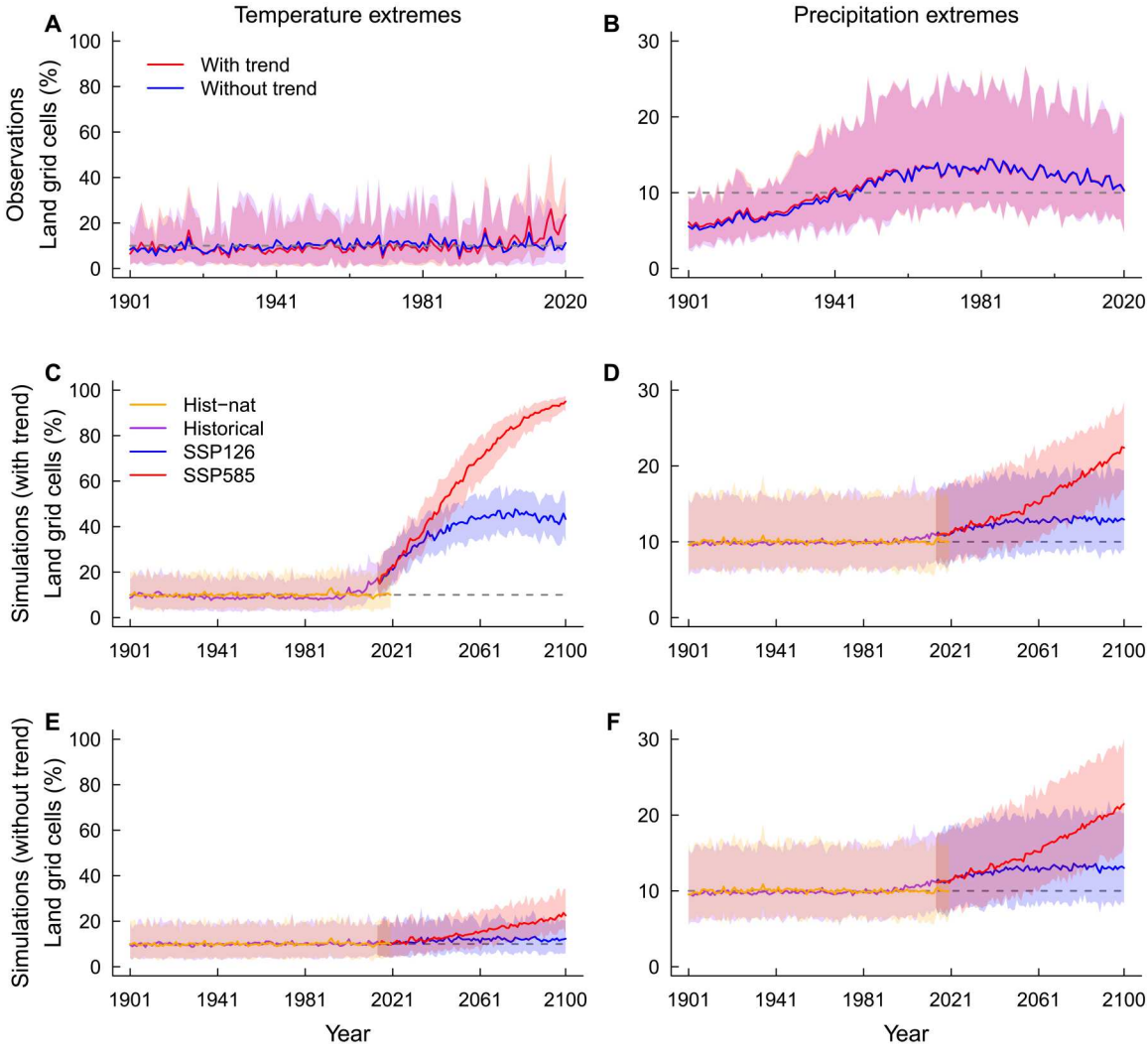


**Fig. 1. Prevalence of concurrent climate extremes over land.** (**A** and **B**) Proportion of land grid cells experiencing monthly temperature and precipitation extremes during the period of 1901–2020 using observations. Climate extremes are identified using temperature (precipitation) data with and without long-term trends, which are determined as the mean temperature (precipitation) of a 20-year moving window. The solid lines show the mean monthly proportion, and the upper and lower bounds of the shading indicate the maximum and minimum monthly proportions, i.e., the greatest departure from the expected proportion (10%, gray dashed lines) when occurrence of climate extremes is independent among different grid cells, for each year. (**C** to **F**) Same as (A) and (B) but using monthly temperature and precipitation data during 1901–2100 with (C and D) and without (E and F) long-term trends from hist-nat, historical, SSP126, and SSP585 simulations of 11 GCMs in CMIP6. The mean, maximum, and minimum proportions shown in the figure represent the mean values of observations and the 11 GCMs, respectively.

climate extremes. This concurrence probability ($p_1$) is compared to the probability ($p_0 = 0.005$) had climate extremes occurred independently for each pair of grid cells, to obtain a probability multiplication factor (PMF), i.e., $p_1/p_0$, which is used to measure the spatial concurrence strength of climate extremes at the grid scale. PMF greater than 1.8 would indicate dependent climate extremes at the 0.05 significance level for a period of 120 years or 1440 months (fig. S3 and Materials and Methods). We also assess each pair among the 44 AR6 land regions to obtain the mean grid cell–based PMF for dependent climate extremes at the regional scale (Fig. 2) and calculate the global mean PMF across all dependent grid cell pairs.

Temperature extremes tend to co-occur positively, with the mean PMF of 3.25 across 58% of land grid cell pairs, while the negative dependence of temperature extremes is only detected across 15% of grid cell pairs. The positive concurrence strength is especially strong over neighboring regions (close to the diagonal in Fig. 2B) and decreases with the distance between regions (Fig. 3A). As a result of global warming, high PMF is also found over many far distant regions, where the PMF is reduced considerably without the warming trends (Fig. 3A and fig. S4A). We also find evidence to indicate stronger positive concurrence in the tropics and higher latitude regions in both hemispheres (Fig. 3E). The strong positively dependent temperature extremes in the tropics are largely driven by the warming trends (Fig. 2B and fig. S5B), and the mean PMF is reduced from 5.4 to 4.5 (18°S-18°N) when the temperature trends are removed (Fig. 3E). The observed negative dependence of temperature extremes is found mainly in the northern mid- and high-latitude regions (Figs. 2C and 3E). Without the

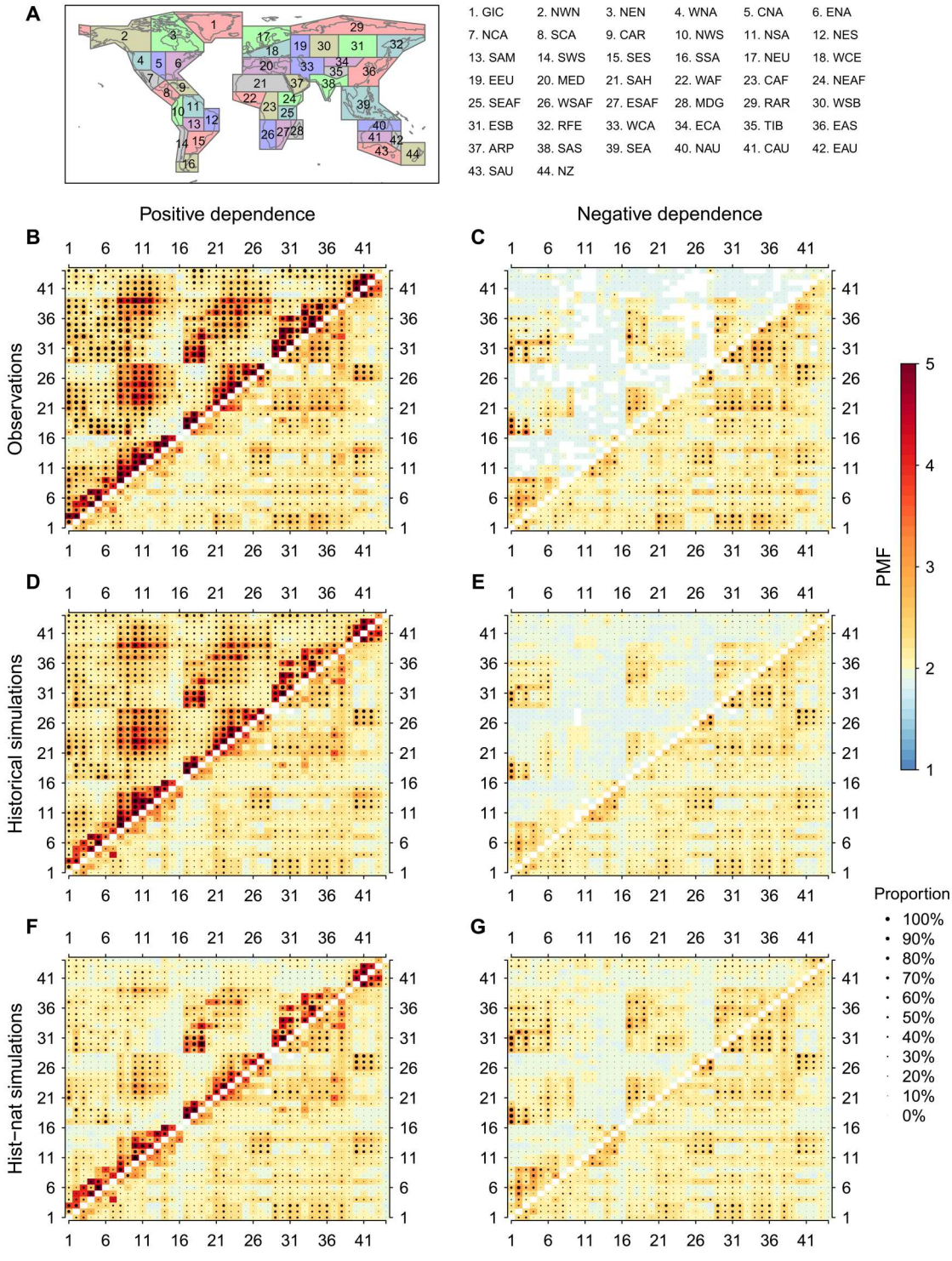


**Fig. 2. Global pattern of spatially concurrent climate extremes based on observations and CMIP6 simulations.** (**A**) IPCC AR6 climate reference land regions (excluding Antarctica). See table S2 for detailed information on these regions. (**B** and **C**) The mean PMF for positively (B) and negatively (C) dependent climate extremes between AR6 regions (top-left triangle, temperature extremes; bottom-right triangle, precipitation extremes) using observations for 1901–2020. Label refers to AR6 regions from 1 to 44. Stippling denotes the proportion of grid cell pairs in which climate extremes are tested to be significantly dependent for each AR6 region pair. (**D** to **G**) Same as (B) and (C) but for historical (D and E) and hist-nat (F and G) simulations of 11 GCMs in CMIP6.

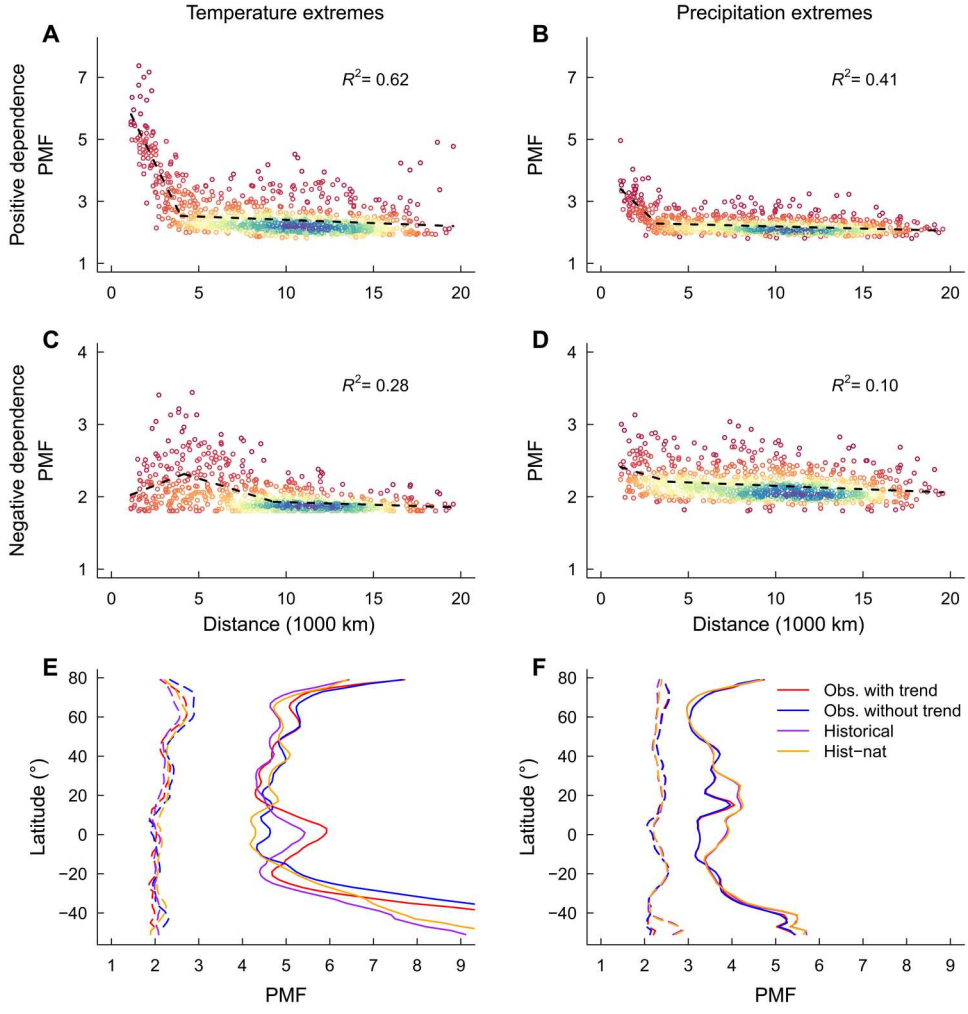


**Fig. 3. Geographical distributions of spatially concurrent climate extremes.** (**A** to **D**) Decrease in regional PMF of climate extremes with increase in the distance between the centers of each region pair based on observations during 1901–2020. Center location of these AR6 regions is listed in table S2. The spectral color shows the density of points, with higher density in blue/purple and lower density in red. The coefficient of determination ($R^2$) for the segmented linear regression is shown for each panel. (**E** and **F**) Latitudinal distributions of PMF for climate extremes using observations with and without long-term trends and the historical and hist-nat simulations from CMIP6 during 1901–2020. The latitudinal distribution is represented by the mean PMF between grid cell pairs within each 10° moving zonal band at 2° increment (Materials and Methods). The solid and dashed lines refer to positively and negatively dependent climate extremes, respectively.

warming trend, we find higher PMF and larger spatial extent of negatively dependent temperature extremes (Fig. 2C and fig. S5C), indicating that global warming shifts land grid cells with negative dependence toward positive dependence.

Precipitation extremes co-occur both positively and negatively, and the positive and negative dependence is detected across 27% and 25% of land grid cell pairs, with mean PMFs of 2.64 and 2.40, respectively. In many of these grid cell pairs, precipitation time series follow the Student's *t* copula with both positive and negative tail dependence (see fig. S6 for an example). We also find consistent spatial patterns of positively and negatively dependent PMF at the regional scale (Fig. 2, B and C), with a correlation coefficient of 0.67. Both spatial patterns show higher PMF of precipitation extremes for neighboring regions and higher latitude regions in the two hemispheres (Fig. 3, B, D, and F). The global pattern of concurrent precipitation extremes is consistent using precipitation with and without long-term trends (Fig. 2, B and C, and fig. S5, B and C), suggesting that the observed co-occurrence of precipitation extremes is mainly associated with the spatial dependence structure of precipitation, with little influence of precipitation trends.

The modeled historical pattern of regional PMF derived from each GCM and particularly from the 11-GCM ensemble matches the observed pattern well ($r$ = 0.81 to 0.95; Fig. 2, B to E, and fig. S7, C and D), indicating that the GCM ensemble realistically represents the global pattern of concurrent climate extremes. The spatial dependence of climate extremes is also detected for ~50% of land grid cell pairs in the hist-nat ensemble (Fig. 2, F and G). As the anthropogenic climate forcing is not included in the hist-nat simulations, the identified spatial dependence of climate extremes is largely driven by the internal climate variability, such as large-scale atmospheric and ocean modulations. The proportion of positively dependent regions and the mean PMF for temperature extremes from the hist-nat ensemble are much lower than that in the historical ensemble (Fig. 2, D and F). This anthropogenic

forcing–induced increases in the mean PMF are tested to be statistically significant (Student's $t$ test, $P < 0.05$) over at least 9 of the 11 GCMs for 56% of 946 global region pairs (Fig. 4C). We also note that the difference between the historical and hist-nat ensembles largely resembles the observed difference in regional PMF obtained with and without temperature trends (Fig. 4). When the long-term temperature trends are removed, the global pattern of positively dependent temperature extremes from the observations and those from the historical and hist-nat simulations are highly consistent ($r > 0.96$; fig. S5, B, D, and F). The anthropogenic warming trends are therefore largely responsible for the observed increasing concurrence strength of temperature extremes. In contrast, we find minimal differences in the regional PMF for precipitation extremes between the historical and hist-nat ensembles (Fig. 4, C and D). This suggests that the spatial co-occurrence of precipitation extremes has not been significantly ($P > 0.05$) affected by the anthropogenic climate forcing over the period 1901–2020.

## Projected increases in global concurrent climate extremes

To understand future changes in global concurrent climate extremes, we split the historical and future (SSP126 and SSP585) simulations into two 100-year periods, historical (1901–2000) and future (2001–2100) periods, and use the historical thresholds to define climate extremes for both periods. In future simulations, all grid cells exhibit strong positive dependence of temperature extremes due to the global warming trends (Fig. 5A), while negative dependence is seldom detected (<3% of grid cell pairs in SSP585). Compared to the historical ensemble, the global PMF of positively dependent temperature extremes increases from 3.2 to 40.7 in SSP126 and to 88.9 in SSP585. Future increases in the regional PMF for positively dependent temperature extremes is stronger across the tropics than other regions in both SSP126 and SSP585 (Fig. 5, A and D). Unlike global temperature extremes that tend to co-occur positively instead of negatively in the future, the PMFs of both positively and negatively dependent precipitation extremes increase across almost all region pairs (Fig. 5, B and C), as increased precipitation variability leads to increased probability of precipitation thresholds being exceeded (fig. S2). At the same time, we find a twofold increase in the spatial extent (i.e., proportion of global grid cell pairs) of positively and negatively dependent precipitation extremes in SSP126 and a threefold increase in SSP585, compared to the proportion of ~20% in the historical period. Increases

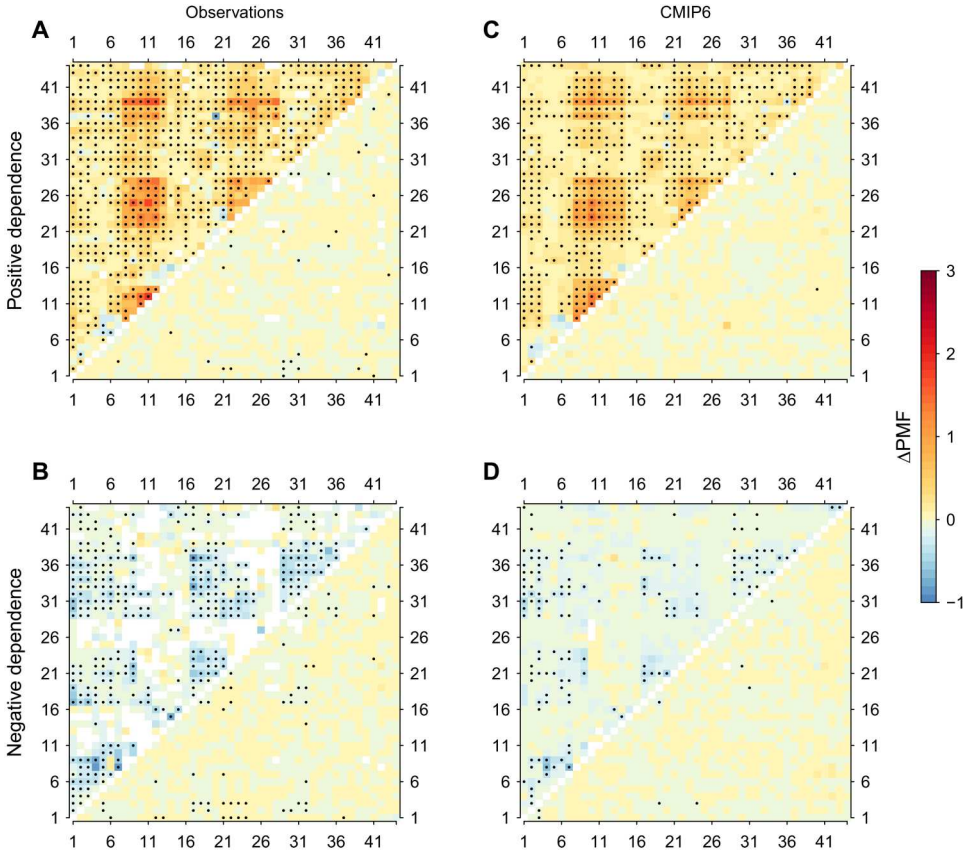


**Fig. 4. Influence of anthropogenic climate change on PMF in observations and CMIP6.** (**A** and **B**) Difference in regional PMF between observations with (Fig. 2, B and C) and without (fig. S5, B and C) long-term trends for positively (A) and negatively (B) dependent climate extremes (top-left triangle, temperature extremes; bottom-right triangle, precipitation extremes) during 1901–2020. Stippling denotes that the difference in PMF is significant at the 95% confidence level (Student's $t$ test), and the sign of the difference is the same for all datasets. (**C** and **D**) Same as (A) and (B) but for the difference between historical (Fig. 2, D and E) and hist-nat (Fig. 2, F and G) simulations for positively (C) and negatively (D) dependent climate extremes during 1901–2020 based on 11 GCMs in CMIP6. Stippling denotes that the difference in PMF is significant at the 95% confidence level (Student's $t$ test), and the sign of the difference is consistent with the sign of multimodel means (as shown in the figure) for at least 9 of the 11 GCMs.

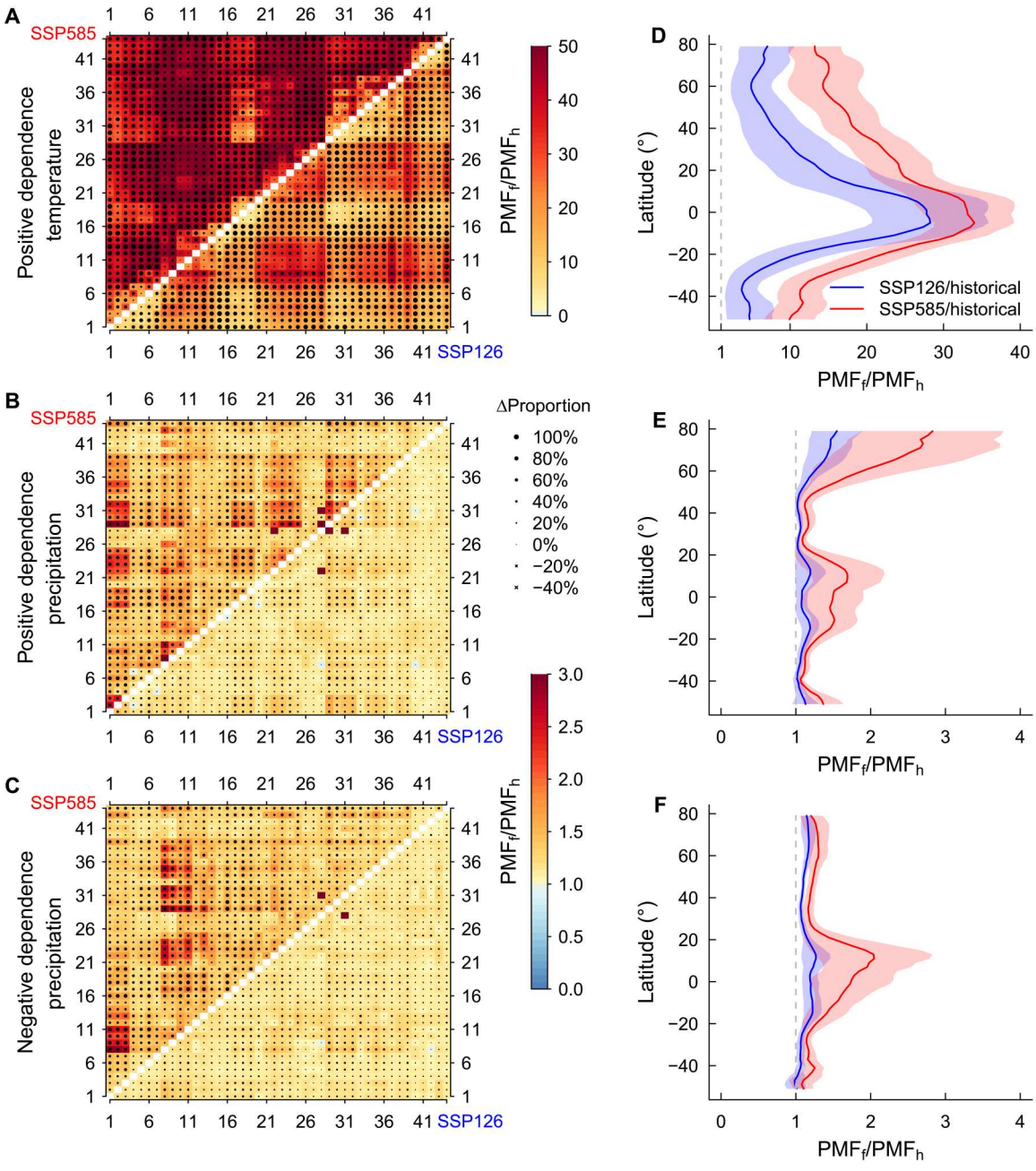


**Fig. 5. Projected increases in global concurrent climate extremes in CMIP6.** (**A** to **C**) Ratio of regional PMF in SSP126 and SSP585 (2001–2100, top-left triangle, SSP585; bottom-right triangle, SSP126) over historical (1901–2000) simulations ($PMF_f/PMF_h$). Climate extremes are identified according to historical thresholds for both periods. Stippling denotes changes in the proportion of grid cell pairs in which climate extremes are tested to be positively or negatively dependent in each AR6 region pair. (**D** to **F**) Latitudinal distribution of $PMF_f/PMF_h$ between grid cell pairs within each 10° moving zonal band at 2° increment in SSP126 and SSP585 relative to historical simulations. The solid lines are multimodel mean of $PMF_f/PMF_h$, and the shading shows the SD of $PMF_f/PMF_h$ across the 11 GCMs in CMIP6.

in the co-occurrence strength and spatial extent of positively dependent precipitation extremes are particularly strong across northern high-latitude regions, while tropical regions are projected to experience large increases in both positively and negatively dependent precipitation extremes due to future increases in precipitation variability (Fig. 5, E and F, and fig. S2). Increases of concurrent precipitation extremes, particularly in these high-risk regions, are much stronger in SSP585 than in SSP126, emphasizing that the low-forcing scenario can substantially curb future increases in global concurrent climate extremes.

Increases of global concurrent climate extremes are largely driven by anthropogenic warming trends and increased climate variability, but may also arise from strengthening spatial dependence of climate extremes. To examine future changes in the spatial dependence, we redefine climate extremes according to thresholds in historical and future simulations separately. This would also allow us to

assess changes in the intensity of climate extremes. Comparison of the thresholds indicates that both extreme high and low temperature are projected to become warmer globally, with greater warming over boreal regions as a result of arctic amplification (fig. S8, A to D) (*36*). We also find increases in the co-occurrence strength and spatial extent of positively dependent temperature extremes, which are particularly evident over tropical and boreal regions (fig. S9, A and E). Concomitantly, negatively dependent temperature extremes reduce greatly around the globe (fig. S9, B and F). This suggests a tendency of negative spatial dependence of temperature extremes to shift toward positive spatial dependence due to anthropogenic climate forcing. Changes in the spatial dependence of precipitation extremes are weaker, but the intensity of precipitation extremes increases greatly in future simulations (figs. S8, E to H, and S9, C and D). Extreme high precipitation increases across 90% of land grid cells, especially over wet regions of the tropics (except the Amazon) and northern high latitudes; over the tropical and mid-latitude regions, extreme low precipitation also becomes more extreme, with lower thresholds indicating larger drought risks (fig. S8, E to H). Overall, future increases in the intensity, co-occurrence strength, and spatial extent of climate extremes suggest increasing risks of concurrent climate extremes caused by anthropogenic climate forcing to the end of this century.

## DISCUSSION

Our analysis of observations and model simulations consistently shows a strong spatial dependence of climate extremes. This has led to frequently concurrent climate extremes in different parts of the world. We find that the global pattern of spatial dependence of climate extremes, which is also evident in the historical simulations with natural forcing only, primarily arises from the internal climate variability. This is because regional climates around the globe are interconnected through teleconnections, and the global drivers of atmospheric variability, such as the El Niño–Southern Oscillation, can bring about climate extremes simultaneously in far distant regions (*37*). The strong spatial co-occurrence of temperature extremes over tropical regions is probably driven by the warm phases of the Pacific Decadal Oscillation (*38*), while concurrent climate extremes in the mid- and high-latitude regions are likely related to Rossby wave patterns (*13*, *39*). We also demonstrate that anthropogenic climate forcing has greatly enhanced the spatial co-occurrence strength of temperature extremes over 56% of global region pairs and will continue to increase the frequency, intensity, and extent of co-occurring climate extremes over global land regions, particularly in the tropics and northern high latitudes. Future amplification of global concurrent climate risks is especially strong in high-end forcing SSP585, while the ambitious emissions mitigation pathway of SSP126 substantially moderates future exacerbation of concurrent climate extremes, especially for the high-risk regions.

While our study has clearly identified the impacts of natural climate variability and anthropogenic climate change on global concurrent climate extremes, the analysis may inherit uncertainties from model simulations. To reduce this uncertainty, we use the 11-GCM ensemble, which agrees with the observations better than individual GCMs (fig. S7). We also note that the initial conditions of model simulations may affect the internal variability in the climate system, and this can lead to uncertainties in the attribution of spatial concurrence of climate extremes to anthropogenic climate change and natural climate variability. To account for the effect of initial conditions, we consider CanESM5 and MIROC6 with a large number of realizations that differ in the initial conditions only for meaningful statistical analysis. We find small variations in the global mean PMF (1 SD < 0.05) and the proportion of dependent regions (1 SD < 0.04) among the 25 realizations of CanESM5 and 50 realizations of MIROC6 (fig. S10, A to D). The interregion dependence based on the first realization used in this study is strongly correlated with that based on the multi-realization mean for both PMF and proportion and for both historical and hist-nat simulations ($r$ = 0.88 to 0.99; fig. S10, E to H). We therefore conclude that the initial conditions have a limited impact on the spatial dependence of climate extremes for the GCMs considered. Although our study identifies the global pattern of concurrent climate extremes associated with natural climate variability and anthropogenic climate change, the physical mechanisms that are responsible for the spatial dependence of climate extremes in each pair of dependent regions are not fully understood. Future work is needed to elucidate the underlying mechanisms, such as atmospheric teleconnections (*13*, *37*) and land-atmosphere interactions (*40*, *41*), to support predictability and management of spatially concurrent climate extremes.

The increasing global concurrent climate extremes pose large risks to our society and ecosystems. In particular, the strongest increases in the past and projected future concurrent temperature extremes occur in tropical regions, where many developing countries have been mostly affected by climate change and are probably the least able to afford the consequences of future increases in temperature extremes (*42*). Increasingly co-occurring temperature extremes will also weaken the capability of tropical biomes to act as the largest terrestrial carbon sink (*43*) and further amplify global climate change. At the same time, increasing precipitation variability and concurrent precipitation extremes will cause more droughts and floods simultaneously, particularly in tropical and northern high-latitude regions, making the adaption to future climate change more difficult. Even if the ambitious climate mitigation targets such as those simulated in SSP126 are ultimately achieved, climate extremes are still projected to greatly increase compared to historical conditions. The increasing concurrent climate extremes and their severe impacts demand urgent international actions to reduce emissions of greenhouse gases and limit climate change impacts. Long-term mitigation and adaptation strategies are needed to deal with the elevated risk arising from increased frequency, intensity, and spatial extent of climate extremes (*44*).

In summary, our study identifies the global pattern of concurrent climate extremes and indicates an increasing risk of global concurrent climate extremes enhanced by historical climate change and will be exacerbated by future anthropogenic climate forcing. Global patterns of the spatial dependence in the past and future show the high-risk regions for concurrent climate extremes, which have far-reaching implications for managing the risks of climate extremes across different regions. Although future risks of climate extremes vary geographically, they are becoming more strongly interlinked through further warming with increased climate variability and spatial dependence of climate extremes. Our understanding of the global pattern of concurrent climate extremes and their responses to different levels of anthropogenic forcings will inform effective

mitigation and adaptation strategies to enable better preparation for future climate extremes.

## MATERIALS AND METHODS

### Observational climate products

We used global climate observations to assess global concurrent climate extremes. We used the CRU TS (Climatic Research Unit gridded Time Series v4.05) dataset, which provides long-term monthly temperature and precipitation observations with a high spatial resolution of 0.5° over land regions (excluding Antarctica) (*31*). The CRU TS dataset has been widely used since its first publication in 2000, and the recent version (v4.05) has been updated to span 1901–2020. It was produced by interpolating monthly climate anomalies from extensive networks of weather station observations onto 0.5° × 0.5° land grids using angular-distance weighting (*31*). The implementation of angular-distance weighting improved interpolation efficiency and accuracy and the traceability between gridded values and the input observations.

We also used observed monthly temperature from the BE surface temperature project (*32*) and monthly land surface precipitation from Global Precipitation Climatology Centre (GPCC) (*33*). The BE surface temperature project provides gridded global temperature anomaly produced by merging weather station thermometer measurements from 14 databases. BE used an automated geostatistical approach to detect local inhomogeneities in temperature time series, and split the records into separate slices, and used a statistical framework that allows for short and discontinuous temperature records to be included to obtain average temperatures (*45*). The framework used the Kriging interpolation to obtain temperature for global land coverage, which is a well-established statistical technique for interpolation and has been widely used. The BE project provides land surface temperature spanning 1753 to 2020 at the spatial resolution of 1° × 1°.

We used GPCC Full Data Monthly Precipitation Product at 1° × 1° (version 2020) (*33*). This version was produced by superimposing gridded monthly precipitation anomalies on the GPCC Precipitation Climatology version 2020, which incorporated data from 84,800 stations with climatological averages. The anomalies were spatially interpolated by using a modified version of the robust empirical interpolation method SPHEREMAP that is preferred by GPCC (*46*). The monthly precipitation product has been extended to cover the entire period from 1891 to 2019 and will be updated at irregular time intervals after substantial database improvements.

These observational climate data were used to assess spatially concurrent climate extremes over land during the historical (1901–2020) period. To facilitate comparisons across observational and modeling datasets, all data were bilinearly interpolated to a common 2° × 2° grid, and the grid cells with the fraction of land higher than 30% were used for data analysis. To identify the climate extremes, we accounted for the effect of seasonal cycle by removing the mean monthly values during the study period 1901–2020 from monthly temperature and precipitation data to obtain their monthly anomalies. These climate anomalies were used to identify climate extremes and calculate the concurrence strength of climate extremes at the grid, regional, and global scales.

### CMIP6 climate outputs

We used climate simulations from the latest state-of-the-art climate models that participate in CMIP6 (*34*) to assess the past and projected future concurrent climate extremes.

In CMIP6, we used the historical simulations (1850–2014) with radiative forcing from both human-induced emissions (greenhouse gases and aerosols) and natural forcing (volcanic and solar activity), and historical simulations with natural forcing only (hist-nat, 1850–2020). We also used model projections of two SSPs (2015–2100): the low forcing sustainability pathway SSP126 (+2.6 W $m^{-2}$ imbalance) and the high-end forcing pathway SSP585 (+8.5 W $m^{-2}$ imbalance). For our analysis, we used 11 GCMs that archive monthly temperature and precipitation data of all four simulations (historical, hist-nat, SSP126, and SSP585). For each model, we extracted monthly near-surface air temperature ("tas") and total precipitation ("pr") from the first ensemble member (table S1), as simulations from different ensemble members of each model are similar (fig. S10). From CanESM5 and MIROC6, we extracted all ensemble members, 25 and 50, respectively, to assess the effect of initial conditions on the spatial dependence of climate extremes. Consistent with observational products, we removed the mean monthly values during the period of 1901–2020 from monthly temperature and precipitation data to eliminate the effect of climate seasonality and obtain monthly anomalies of temperature and precipitation.

### Spatial concurrence of climate extremes

We proposed a statistical framework to assess the spatial concurrence of climate extremes at the grid, regional, and global scales. To define climate extremes, we used a simple and straightforward approach by counting the number of months in which the climate anomalies exceed a percentile-based threshold. Temperature (precipitation) extremes are defined as months when temperature (precipitation) anomalies are above their 95th percentile or below their 5th percentile over the study period. This percentile-based definition allows comparable extreme thresholds across different climates, regions and periods, and identification and quantification of the co-occurrence strength of climate extremes at different locations.

The concurrence probability of climate extremes is largely affected by the spatial dependence (correlation) of climate variables. For example, we consider the time series of temperature anomalies at two grid cells, $G_i$ and $G_j$, and transform them into normalized ranks as $g_i$ and $g_j$, respectively. If $G_i$ and $G_j$ are positively correlated, extreme high (low) temperatures tend to occur in the same month, and the probability of positively concurrent temperature extremes at two grid cells, $P^+(G_i, G_j)$, is expressed as

$$P^+(G_i, G_j) = P[(g_i > 0.95 \cap g_j > 0.95) \text{ or } (g_i < 0.05 \cap g_j < 0.05)], i \neq j \quad (1)$$

As the concurrence probability of temperature extremes generally increases with the correlation strength (*5*, *11*), the stronger the correlation $r(G_i, G_j)$, the higher the probability $P^+(G_i, G_j)$. Therefore, $P^+(G_i, G_j)$ is expected to be higher than that if $G_i$ and $G_j$ are independent ($P_0 = 0.05 \times 0.05 \times 2 = 0.005$).

On the other hand, if $G_i$ and $G_j$ are negatively correlated, extreme high temperature for one grid cell would co-occur with extreme low temperature at the other grid cell. In this case, the probability of negatively concurrent temperature extremes at the two grid cells,

$P^-(G_i, G_j)$, is given by

$$P^-(G_i, G_j) = P[(g_i > 0.95 \cap g_j < 0.05) \text{ or } (g_i < 0.05 \cap g_j > 0.95)], i \neq j \quad (2)$$

Similarly, $P^-(G_i, G_j)$ is also expected to be higher than $P_0 = 0.005$ and decreases with $r(G_i, G_j)$.

It is also possible that $G_i$ and $G_j$ are positively or negatively correlated, but their extremes do not positively or negatively co-occur, for example, $P^+(G_i, G_j)$ or $P^-(G_i, G_j) < 0.005$, which may be caused by the so-called tail independence (*47*). In contrast, tail dependence in extreme deviations may also occur when $G_i$ and $G_j$ are not correlated. To account for the effect of tail (in)dependence, we directly tested the dependence of temperature extremes for each pair of grid cells. To identify whether temperature extremes are significantly positively and mutually dependent at two grid cells, we tested the following hypothesis:

1) The null hypothesis is that temperature anomalies at two grid cells are independent; therefore, for each month $k$, the probability of positively concurrent temperature extremes at the two grid cells equals 0.005 ($P = 0.005$).

$$p = P[(g_i > 0.95 \cap g_j > 0.95) \text{ or } (g_i < 0.05 \cap g_j < 0.05)] \quad (3)$$

The alternative hypothesis is that temperature extremes are positively dependent, namely, $P > 0.005$.

2) To test the null hypothesis, we construct a test statistic: the number of months ($m$) of all assessed months ($n$) that temperature extremes positively co-occur at the two grid cells.

3) If we assume that the occurrence of temperature extremes at two grid cells is independent for different months, the number of such concurrences would follow the binomial distribution. The probability of positively dependent temperature extremes that occur exactly $m$ times in $n$ months, $P_m$, is given by

$$P_m = \frac{n!}{m!(n-m)!} p^m q^{n-m}, p = 0.005, q = 0.995 \quad (4)$$

According to the probability density function of the binomial distribution, if the positively dependent temperature extremes occur ≥13 times in the historical period (1901–2020, $n$ = 1440), which corresponds to a probability of >0.009 (or ≥13 of 1440), we can reject the null hypothesis ($P$ <0.05; fig. S3). In this case, extreme high and low temperatures at the two grid cells are positively co-dependent at a confidence level of 95%.

4) Otherwise, if the null hypothesis cannot be rejected, temperature extremes do not significantly positively co-occur.

We also performed similar hypothesis testing for negatively dependent temperature extremes at the grid scale and used the statistical method to identify the spatial concurrence of precipitation extremes as well. For each grid cell pair where climate extremes positively or negatively co-occur at the confidence level of 95%, we measured the concurrence probability of climate extremes at the two grid cells. To quantify the spatial concurrence strength, we calculated PMF, which is defined as the ratio of the concurrence probability of climate extremes at two grid cells over that if climate extremes occurred independently in each grid cell ($P_0 = 0.005$)

$$PMF_{i,j} = \frac{P(G_i, G_j)}{P_0} \quad (5)$$

where $P(G_i, G_j)$ here represents both $P^+(G_i, G_j)$ for grid cell pairs where climate extremes are tested to be positively dependent and $P^-(G_i, G_j)$ for negatively dependent climate extremes. Accordingly, climate extremes between two grid cells are significantly and mutually dependent when PMF is greater than 1.8 (0.009/0.005).

At the regional scale, we assessed the co-occurrence strength of climate extremes among the 44 IPCC AR6 land regions. For each AR6 region pair, we calculated PMF of each pair of grid cells in the two regions where climate extremes positively or negatively co-occur and obtained separately the mean PMF for positively and negatively co-occurring climate extremes at the regional scale. The mean PMF for each region pair is expressed as

$$PMF_{R_m,R_n} = \frac{\overline{P(G_i, G_j)}}{P_0}, i \varepsilon R_m, j \varepsilon R_n \quad (6)$$

where $\overline{P(G_i, G_j)}$ is the mean of $P(G_i, G_j)$ of grid cell pairs in the two regions $R_m$ and $R_n$.

To capture the latitudinal distribution of PMF, we obtained the mean PMF across grid cells for a moving 10° zone at 2° increment, i.e., from latitude −90° to −80°, −88° to −78°, etc.

$$PMF_{L_m} = \frac{\overline{P(G_i, G_j)}}{P_0}, i, j \varepsilon L_m, i \neq j \quad (7)$$

where $m$ refers to the center of each 10° zone that varies from −85° to 85°, again at 2° increment.

The global mean PMF was calculated across land grid cells where climate extremes positively or negatively co-occur.

$$PMF_{Land} = \frac{\overline{P(G_i, G_j)}}{P_0}, i, j \varepsilon Land, i \neq j \quad (8)$$

For data analysis, we used the observations and CMIP6 model simulations to identify the spatial concurrence of climate extremes in the historical period (1901–2020). We first tested the hypothesis of spatial independence of temperature extremes and precipitation extremes individually for each pair of grid cells. Temperature extremes are either positively or negatively dependent in most land grid cell pairs, while precipitation extremes at two grid cells can be positively or negatively dependent or both positively and negatively dependent when precipitation time series follow the Student's $t$ copula with both positive and negative tail dependence (fig. S6). For grid cell pairs where climate extremes positively or negatively co-occur at the confidence level of 95%, we calculated the mean PMF and the proportion of grid cell pairs for positively and negatively dependent climate extremes at the regional and global scales using the above statistical framework. The mean PMF and proportion from observational products and from the 11 GCMs were used to assess the global pattern of concurrent climate extremes (Fig. 2). We also examined the consistency of the mean PMF and proportion between observations and GCMs at the regional and global scales (fig. S7).

### Influence of anthropogenic climate change on concurrent climate extremes

We combined observational products and CMIP6 model simulations to identify whether and how much anthropogenic climate change has affected the spatial co-occurrence of climate extremes. Anthropogenic climate forcing generally influences climate

extremes through changes in the mean or variability or both. In addition to local climate change, co-occurring climate extremes in different regions also rely on the spatial dependence structure of climate variables (*4*). Therefore, anthropogenic climate change may strengthen or weaken the spatial dependence of climate variables to further amplify or moderate concurrent climate extremes.

We first identified the impact of historical climate trends on global concurrent climate extremes using observed temperature and precipitation with and without long-term trends during 1901–2020. Considering that the climate trends may not be linear, we removed the nonlinear trends in temperature and precipitation determined as the mean values of a 20-year moving window. These observations were also used to obtain the global pattern of PMF across the IPCC AR6 climate regions and the latitudinal distribution of PMF to identify the hotspot regions where the spatial co-occurrence of climate extremes was most affected by climate trends.

We also detected the signal of anthropogenic climate forcing on historical concurrent climate extremes by comparing historical simulations with and without (hist-nat) anthropogenic forcing from the 11 GCMs of CMIP6. As the historical simulations end in 2014, we extended the historical simulations with those from the SSP585 simulations, which closely tracks the recent emissions trajectory, until 2020 to match the observational record period for each model. We also extended historical simulations with the SSP126 simulations, and the results are very similar (Fig. 1, C to F). For regional analysis, we obtained PMF across the IPCC AR6 land regions and compared the regional PMF between historical and hist-nat simulations to identify region pairs where the difference in PMF is significant at the 95% confidence level (Student's *t* test). Given that anthropogenic climate forcing may affect regional PMF in either positive or negative manner, we further tested whether the sign of multimodel mean difference in PMF is statistically consistent. The null hypothesis is that if the impact of anthropogenic climate forcing on regional PMF is random and independent, then it would be equally likely to have a positive or negative difference in PMF. Using the binomial distribution, we can reject the null hypothesis at a significance level of 0.05 if no less than 9 of the 11 GCMs agree in terms of the sign of the mean difference in PMF.

$$P(m \geq 9) = \sum_{m=9}^{11} \frac{11!}{m!(11-m)!} 0.5^m \times 0.5^{11-m} < 0.05 \quad (9)$$

We identified all region pairs where anthropogenic climate forcing has led to significant impacts on spatially concurrent climate extremes if the difference in PMF between historical and hist-nat simulations is significant at the 95% confidence level (Student's *t* test) and the sign of the difference is consistent with the sign of the multimodel means for at least 9 of the 11 GCMs (Fig. 4, C and D).

To assess the impact of future climate change on the risk of global concurrent climate extremes, we compared the projected spatial co-occurrence of climate extremes in SSP126 and SSP585 to historical simulations. In CMIP6, SSP585 tracks the recent emissions trajectory, while SSP126 represents the ambitious mitigation targets of the Paris Agreement. This comparison allows us to quantify future risks of co-occurring climate extremes for different forcing levels and evaluate the benefits of implementing climate mitigation measures. To examine the impact of future anthropogenic forcing on concurrent climate extremes, we split the whole period into two 100-year periods and defined climate extremes according to (i) historical (1901–2000) thresholds and (ii) separate thresholds for each of historical (1901–2000) and future (2001–2100) periods to determine the influence of anthropogenic climate forcing on the spatial co-occurrence strength of climate extremes and, especially, on the spatial dependence of climate extremes. We also compared the thresholds of climate extremes in (ii) to assess future changes in the intensity of concurrent climate extremes.

### Influence of natural climate variability on concurrent climate extremes

Global concurrent climate extremes may also be affected by natural climate variability, such as large-scale atmospheric and ocean modulations. The influence of natural climate variability on global concurrent climate extremes can be assessed using the hist-nat simulations with natural forcing only, in which the anthropogenic climate forcing is not included and the detected spatial concurrence of climate extremes is largely driven by natural climate variability. However, the natural climate variability and its influence on global concurrent climate extremes may be sensitive to models selected and the initial conditions of model simulations. Therefore, we used the hist-nat ensemble from the 11 GCMs of CMIP6 to assess the influence of natural climate variability on historical concurrent climate extremes at the global and regional scales and evaluated the influence of initial conditions on concurrent climate extremes using 25 realizations from CanESM5 and 50 realizations from MIROC6. These realizations differ in the initial conditions only.

### Sensitivity of spatial dependence to the definition of climate extremes

We tested the sensitivity of spatial dependence to the threshold used to define climate extremes. We calculated the global mean PMF and the proportion of land grid cell pairs with dependent climate extremes using observations and a series of probability thresholds of 0.01/0.99, 0.02/0.98, 0.03/0.97, ....., 0.08/0.92, 0.09/0.91, 0.1/0.9 for hypothesis testing. The global mean PMF of dependent climate extremes increases, while the proportion of dependent grid cell pairs decreases with more extreme thresholds (fig. S11, A to D), indicating that the spatial dependence of concurrence is strengthened but the number of region pairs is reduced using stricter criteria for climate extremes. We also obtained the global pattern of concurrent climate extremes across the 44 AR6 regions with a smaller tail of 0.01/0.99 and a larger tail of 0.1/0.9 and compared the results to that shown in Fig. 2 (B and C). Although the global patterns of concurrent extremes are broadly consistent using different thresholds, it is evident that the regional PMF is higher, but the proportion of grid cell pairs is lower with a more extreme threshold (fig. S11, E to H).

## Supplementary Materials

**This PDF file includes:**

Figs. S1 to S11
Tables S1 and S2

## REFERENCES AND NOTES

1. A. AghaKouchak, F. Chiang, L. S. Huning, C. A. Love, I. Mallakpour, O. Mazdiyasni, H. Moftakhari, S. M. Papalexiou, E. Ragno, M. Sadegh, Climate extremes and compound hazards in a warming world. *Annu. Rev. Earth Planet. Sci.* **48**, 519–548 (2020).

2. E. M. Fischer, S. Sippel, R. Knutti, Increasing probability of record-shattering climate extremes. *Nat. Clim. Change* **11**, 689–695 (2021).
3. J. Zscheischler, S. Westra, B. J. J. M. van den Hurk, S. I. Seneviratne, P. J. Ward, A. Pitman, A. AghaKouchak, D. N. Bresch, M. Leonard, T. Wahl, X. Zhang, Future climate risk from compound events. *Nat. Clim. Change* **8**, 469–477 (2018).
4. J. Zscheischler, O. Martius, S. Westra, E. Bevacqua, C. Raymond, R. M. Horton, B. van den Hurk, A. AghaKouchak, A. Jézéquel, M. D. Mahecha, D. Maraun, A. M. Ramos, N. N. Ridder, W. Thiery, E. Vignotto, A typology of compound weather and climate events. *Nat. Rev. Earth Environ.* **1**, 333–347 (2020).
5. J. Zscheischler, S. I. Seneviratne, Dependence of drivers affects risks associated with compound events. *Sci. Adv.* **3**, e1700263 (2017).
6. Z. Hao, F. Hao, V. P. Singh, X. Zhang, Changes in the severity of compound drought and hot extremes over global land areas. *Environ. Res. Lett.* **13**, 124022 (2018).
7. O. Mazdiyasni, A. AghaKouchak, Substantial increase in concurrent droughts and heatwaves in the United States. *Proc. Natl. Acad. Sci. U.S.A.* **112**, 11484–11489 (2015).
8. S. Zhou, Y. Zhang, A. P. Williams, P. Gentine, Projected increases in intensity, frequency, and terrestrial carbon costs of compound drought and aridity events. *Sci. Adv.* **5**, eaau5740 (2019).
9. S. Feng, X. Wu, Z. Hao, Y. Hao, X. Zhang, F. Hao, A database for characteristics and variations of global compound dry and hot events. *Weather Clim. Extrem.* **30**, 100299 (2020).
10. M. Leonard, S. Westra, A. Phatak, M. Lambert, B. van den Hurk, K. McInnes, J. Risbey, S. Schuster, D. Jakob, M. Stafford-Smith, A compound event framework for understanding extreme impacts. *Wiley Interdiscip. Rev. Clim. Change* **5**, 113–128 (2014).
11. S. Zhou, A. P. Williams, A. M. Berg, B. I. Cook, Y. Zhang, S. Hagemann, R. Lorenz, S. I. Seneviratne, P. Gentine, Land–atmosphere feedbacks exacerbate concurrent soil drought and atmospheric aridity. *Proc. Natl. Acad. Sci. U.S.A.* **116**, 18848–18853 (2019).
12. A. Sarhadi, M. C. Ausín, M. P. Wiper, D. Touma, N. S. Diffenbaugh, Multidimensional risk in a nonstationary climate: Joint probability of increasingly severe warm and dry conditions. *Sci. Adv.* **4**, eaau3487 (2018).
13. K. Kornhuber, D. Coumou, E. Vogel, C. Lesk, J. F. Donges, J. Lehmann, R. M. Horton, Amplified Rossby waves enhance risk of concurrent heatwaves in major breadbasket regions. *Nat. Clim. Change* **10**, 48–53 (2019).
14. J. E. Overland, Causes of the record-breaking Pacific Northwest heatwave, late June 2021. *Atmosphere* **12**, 1434 (2021).
15. W. Cornwall, Europe's deadly floods leave scientists stunned. *Science* **373**, 372–373 (2021).
16. D. Normile, Zhengzhou subway flooding a warning for other major cities. *Science* , (2021).
17. B. Stone Jr., E. Mallen, M. Rajput, C. J. Gronlund, A. M. Broadbent, E. S. Krayenhoff, G. Augenbroe, M. S. O'Neill, M. Georgescu, Compound climate and infrastructure events: How electrical grid failure alters heat wave risk. *Environ. Sci. Technol.* **55**, 6957–6964 (2021).
18. F. Vahedifard, A. AghaKouchak, N. H. Jafari, Compound hazards yield Louisiana flood. *Science* **353**, –1374 (2016).
19. B. Tellman, J. A. Sullivan, C. Kuhn, A. J. Kettner, C. S. Doyle, G. R. Brakenridge, T. A. Erickson, D. A. Slayback, Satellite imaging reveals increased proportion of population exposed to floods. *Nature* **596**, 80–86 (2021).
20. W. B. Anderson, R. Seager, W. Baethgen, M. Cane, L. You, Synchronous crop failures and climate-forced production variability. *Sci. Adv.* **5**, eaaw1976 (2019).
21. F. Gaupp, J. Hall, S. Hochrainer-Stigler, S. Dadson, Changing risks of simultaneous global breadbasket failure. *Nat. Clim. Change* **10**, 54–57 (2020).
22. A. Toreti, O. Cronie, M. Zampieri, Concurrent climate extremes in the key wheat producing regions of the world. *Sci. Rep.* **9**, 5493 (2019).
23. M. Tigchelaar, D. S. Battisti, R. L. Naylor, D. K. Ray, Future warming increases probability of globally synchronized maize production shocks. *Proc. Natl. Acad. Sci. U.S.A.* **115**, 6644–6649 (2018).
24. D. M. J. S. Bowman, G. J. Williamson, J. T. Abatzoglou, C. A. Kolden, M. A. Cochrane, A. M. S. Smith, Human exposure and sensitivity to globally extreme wildfire events. *Nat. Ecol. Evol.* **1**, 0058 (2017).
25. S.-K. Min, X. Zhang, F. W. Zwiers, G. C. Hegerl, Human contribution to more-intense precipitation extremes. *Nature* **470**, 378–381 (2011).
26. E. M. Fischer, R. Knutti, Anthropogenic contribution to global occurrence of heavy-precipitation and high-temperature extremes. *Nat. Clim. Change* **5**, 560–564 (2015).
27. A. P. Williams, E. R. Cook, J. E. Smerdon, B. I. Cook, J. T. Abatzoglou, K. Bolles, S. H. Baek, A. M. Badger, B. Livneh, Large contribution from anthropogenic warming to an emerging North American megadrought. *Science* **368**, 314–318 (2020).
28. M. C. Kirchmeier-Young, X. Zhang, Human influence has intensified extreme precipitation in North America. *Proc. Natl. Acad. Sci. U.S.A.* **117**, 13308–13313 (2020).
29. A. K. Magnan, H.-O. Pörtner, V. K. E. Duvat, M. Garschagen, V. A. Guinder, Z. Zommers, O. Hoegh-Guldberg, J.-P. Gattuso, Estimating the global risk of anthropogenic climate change. *Nat. Clim. Change* **11**, 879–885 (2021).
30. C. Raymond, L. Suarez-Gutierrez, K. Kornhuber, M. Pascolini-Campbell, J. Sillmann, D. E. Waliser, Increasing spatiotemporal proximity of heat and precipitation extremes in a warming world quantified by a large model ensemble. *Environ. Res. Lett.* **17**, 035005 (2022).
31. I. Harris, T. J. Osborn, P. Jones, D. Lister, Version 4 of the CRU TS monthly high-resolution gridded multivariate climate dataset. *Sci. Data* **7**, 109 (2020).
32. R. Rohde, R. A. Muller, R. Jacobsen, E. Muller, C. Wickham, A new estimate of the average earth surface land temperature spanning 1753 to 2011. *Geoinfor. Geostat. An Overview.* **1**, 1000101 (2013).
33. U. Schneider, A. Becker, P. Finger, E. Rustemeier, M. Ziese, GPCC full data monthly version 2020 at 1.0°: Monthly land-surface precipitation from rain-gauges built on GTS-based and historic data (Deutscher Wetterdienst, 2020).
34. V. Eyring, S. Bony, G. A. Meehl, C. A. Senior, B. Stevens, R. J. Stouffer, K. E. Taylor, Overview of the coupled model intercomparison project phase 6 (CMIP6) experimental design and organization. *Geosci. Model Dev.* **9**, 1937–1958 (2016).
35. M. Iturbide, J. M. Gutiérrez, L. M. Alves, J. Bedia, R. Cerezo-Mota, E. Cimadevilla, A. S. Cofiño, A. Di Luca, S. H. Faria, I. V. Gorodetskaya, M. Hauser, S. Herrera, K. Hennessy, H. T. Hewitt, R. G. Jones, S. Krakovska, R. Manzanas, D. Martínez-Castro, G. T. Narisma, I. S. Nurhati, I. Pinto, S. I. Seneviratne, B. van den Hurk, C. S. Vera, An update of IPCC climate reference regions for subcontinental analysis of climate model data: Definition and aggregated datasets. *Earth Syst. Sci. Data* **12**, 2959–2970 (2020).
36. A. Dai, D. Luo, M. Song, J. Liu, Arctic amplification is caused by sea-ice loss under increasing $CO_2$. *Nat. Commun.* **10**, 121 (2019).
37. H. Steptoe, S. E. O. Jones, H. Fox, Correlations between extreme atmospheric hazards and global teleconnections: Implications for multihazard resilience. *Rev. Geophys.* **56**, 50–78 (2018).
38. H. Yang, S. Piao, C. Huntingford, S. Peng, P. Ciais, A. Chen, G. Zhou, X. Wang, M. Gao, J. Zscheischler, Strong but intermittent spatial covariations in tropical land temperature. *Geophys. Res. Lett.* **46**, 356–364 (2019).
39. C. D. W. Rogers, K. Kornhuber, S. E. Perkins-Kirkpatrick, P. C. Loikith, D. Singh, Sixfold increase in historical northern hemisphere concurrent large heatwaves driven by warming and changing atmospheric circulations. *J. Climate* **35**, 1063–1078 (2022).
40. D. G. Miralles, P. Gentine, S. I. Seneviratne, A. J. Teuling, Land–atmospheric feedbacks during droughts and heatwaves: State of the science and current challenges. *Ann. N. Y. Acad. Sci.* **1436**, 19–35 (2019).
41. T. Sato, T. Nakamura, Intensification of hot Eurasian summers by climate change and land–atmosphere interactions. *Sci. Rep.* **9**, 10866 (2019).
42. C.-F. Schleussner, D. Deryng, S. D'haen, W. Hare, T. Lissner, M. Ly, A. Nauels, M. Noblet, P. Pfleiderer, P. Pringle, M. Rokitzki, F. Saeed, M. Schaeffer, O. Serdeczny, A. Thomas, 1.5°C hotspots: Climate hazards, vulnerabilities, and impacts. *Annu. Rev. Environ. Resour.* **43**, 135–163 (2018).
43. X. Wang, S. Piao, P. Ciais, P. Friedlingstein, R. B. Myneni, P. Cox, M. Heimann, J. Miller, S. Peng, T. Wang, H. Yang, A. Chen, A two-fold increase of carbon cycle sensitivity to tropical temperature variations. *Nature* **506**, 212–215 (2014).
44. L. Berrang-Ford, A. R. Siders, A. Lesnikowski, A. P. Fischer, M. W. Callaghan, N. R. Haddaway, K. J. Mach, M. Araos, M. A. R. Shah, M. Wannewitz, D. Doshi, T. Leiter, C. Matavel, J. I. Musah-Surugu, G. Wong-Parodi, P. Antwi-Agyei, I. Ajibade, N. Chauhan, W. Kakenmaster, C. Grady, V. I. Chalastani, K. Jagannathan, E. K. Galappaththi, A. Sitati, G. Scarpa, E. Totin, K. Davis, N. C. Hamilton, C. J. Kirchhoff, P. Kumar, B. Pentz, N. P. Simpson, E. Theokritoff, D. Deryng, D. Reckien, C. Zavaleta-Cortijo, N. Ulibarri, A. C. Segnon, V. Khavhagali, Y. Shang, L. Zvobgo, Z. Zommers, J. Xu, P. A. Williams, I. V. Canosa, N. van Maanen, B. van Bavel, M. van Aalst, L. L. Turek-Hankins, H. Trivedi, C. H. Trisos, A. Thomas, S. Thakur, S. Templeman, L. C. Stringer, G. Sotnik, K. D. Sjostrom, C. Singh, M. Z. Siña, R. Shukla, J. Sardans, E. A. Salubi, L. S. S. Chalkasra, R. Ruiz-Díaz, C. Richards, P. Pokharel, J. Petzold, J. Penuelas, J. P. Avila, J. B. P. Murillo, S. Ouni, J. Niemann, M. Nielsen, M. New, P. N. Schwerdtle, G. N. Alverio, C. A. Mullin, J. Mullenite, A. Mosurska, M. D. Morecroft, J. C. Minx, G. Maskell, A. M. Nunbogu, A. K. Magnan, S. Lwasa, M. Lukas-Sithole, T. Lissner, O. Lilford, S. F. Koller, M. Jurjonas, E. T. Joe, L. T. M. Huynh, A. Hill, R. R. Hernandez, G. Hegde, T. Hawxwell, S. Harper, A. Harden, M. Haasnoot, E. A. Gilmore, L. Gichuki, A. Gatt, M. Garschagen, J. D. Ford, A. Forbes, A. D. Farrell, C. A. F. Enquist, S. Elliott, E. Duncan, E. C. de Perez, S. Coggins, T. Chen, D. Campbell, K. E. Browne, K. J. Bowen, R. Biesbroek, I. D. Bhatt, R. B. Kerr, S. L. Barr, E. Baker, S. E. Austin, I. Arotoma-Rojas, C. Anderson, W. Ajaz, T. Agrawal, T. Z. Abu, A systematic global stocktake of evidence on human adaptation to climate change. *Nat. Clim. Change* **11**, 989–1000 (2021).
45. R. Rohde, R. Muller, R. Jacobsen, S. Perlmutter, S. Mosher, Berkeley earth temperature averaging process. *Geoinform. Geostat. Overview.* **1**, 1000103 (2013).
46. A. Becker, P. Finger, A. Meyer-Christoffer, B. Rudolf, K. Schamm, U. Schneider, M. Ziese, A description of the global land-surface precipitation data products of the global precipitation climatology centre with sample applications including centennial (trend) analysis from 1901–present. *Earth Syst. Sci. Data* **5**, 71–99 (2013).

47. A. Poulin, D. Huard, A.-C. Favre, S. Pugin, Importance of tail dependence in bivariate frequency analysis. *J. Hydrol. Eng.* **12**, 394–403 (2007).

**Acknowledgments:** We acknowledge the World Climate Research Programme's Working Group on Coupled Modelling, which is responsible for CMIP, and we thank the climate modeling groups (listed in table S1 of this paper) for producing and making available their model output. For CMIP, the U.S. Department of Energy's Program for Climate Model Diagnosis and Intercomparison provides coordinating support and led development of software infrastructure in partnership with the Global Organization for Earth System Science Portals. **Funding:** This work was supported by the National Key Research and Development Program of China (2022YFF0802400), the NSFC Excellent Young Scientists Fund (Overseas), and the Fundamental Research Funds for the Central Universities. **Author contributions:** S.Z. conceived and designed the study. S.Z. processed observational products and model simulations, with the help from Y.Z. B.Y. contributed to data analysis and interpretation. S.Z. drafted the manuscript. All authors edited the manuscript. **Competing interests:** The authors declare that they have no competing interests. **Data and materials availability:** All data used in this study are available online. The CRU temperature and precipitation products are available from https://crudata.uea.ac.uk/cru/data/hrg/. The Berkeley Earth temperature product is available from http://berkeleyearth.org/data/. The GPCC precipitation product is available from https://opendata.dwd.de/climate_environment/GPCC/html/fulldata-monthly_v2020_doi_download.html. The CMIP6 model simulations are available from https://esgf-node.llnl.gov/search/cmip6/. All data needed to evaluate the conclusions in the paper are present in the paper and/or the Supplementary Materials.

Submitted 17 January 2022
Accepted 6 February 2023
Published 10 March 2023
10.1126/sciadv.abo1638